

Ligand Steric Profile Tunes the Reactivity of Indium Phosphide Clusters

Soren F. Sandeno,^a Kyle J. Schnitzenbaumer,^b Sebastian M. Krajewski,^a Ryan A. Beck,^a Dylan M. Ladd,^c Kelsey R. Levine,^c Damara Dayton,^c Michael F. Toney,^{c,d} Werner Kaminsky,^a Xiaosong Li,^a and Brandi M. Cossairt^{a*}

^aDepartment of Chemistry, University of Washington, Box 351700, Seattle, WA 98195-1700, United States

^bDivision of Natural Sciences and Mathematics, Transylvania University, Lexington, Kentucky 40508-1797, United States

^cDepartment of Materials Science and Engineering, University of Colorado, Boulder, Colorado 80309, United States

^dDepartment of Chemical and Biological Engineering, Renewable and Sustainable Energy Institute, University of Colorado, Boulder, Colorado 80309, United States

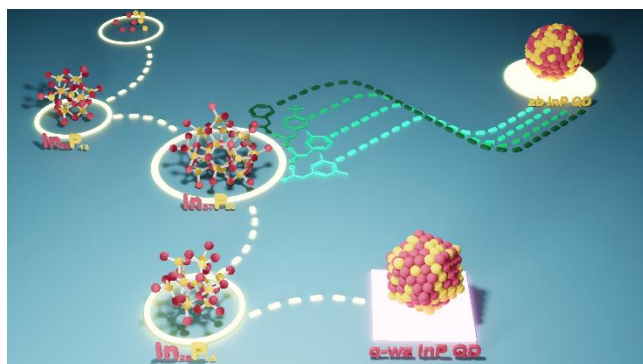
*cossairt@uw.edu

Abstract

Indium phosphide quantum dots have become an industrially relevant material for solid-state lighting and wide color gamut displays. The synthesis of indium phosphide quantum dots from indium carboxylates and tris(trimethylsilyl)phosphine ($\text{P}(\text{SiMe}_3)_3$) is understood to proceed through the formation of magic-sized clusters, with $\text{In}_{37}\text{P}_{20}(\text{O}_2\text{CR})_{51}$ being the key isolable intermediate. The reactivity of the $\text{In}_{37}\text{P}_{20}(\text{O}_2\text{CR})_{51}$ cluster is a vital parameter in controlling conversion to quantum dots. Here, we report structural perturbations to $\text{In}_{37}\text{P}_{20}(\text{O}_2\text{CR})_{51}$ clusters induced by tuning the steric properties of a series of substituted phenylacetate ligands. This approach allows for control over reactivity with $\text{P}(\text{SiMe}_3)_3$, where meta-substituents enhance the susceptibility to ligand displacement and para-substituents hinder phosphine diffusion to the core. Thermolysis studies show that with complete cluster dissolution, steric profile can modulate the nucleation period, whereas partial dissolution from indium carboxylate loss results in conversion

to uniform InP cores with a narrow, 419 nm absorbance. The enhanced stability from ligand engineering also allows for the isolation and structural characterization by single-crystal X-ray diffraction of a new III-V magic-sized cluster with formula $\text{In}_{26}\text{P}_{13}(\text{O}_2\text{CR})_{39}$. This intermediate is thought to precede the $\text{In}_{37}\text{P}_{20}(\text{O}_2\text{CR})_{51}$ cluster on the InP reaction coordinate. The physical and electronic structure of this cluster are analyzed, providing new insight into previously unrecognized relationships between II-VI and III-V materials and the discrete growth of III-V cluster intermediates.

TOC Graphic



Introduction

The development of colloidal quantum dot (QD) syntheses has allowed for control over their attractive optoelectronic properties. Many of these synthetic methods begin empirically with a limited understanding of the underlying nucleation and growth mechanisms. InP QDs have emerged as a commercially relevant, emissive material and as such their formation pathways have been the subject of deep investigation. Today, the state-of-the-art method for producing InP QDs involves the combination of indium carboxylates ($\text{In}(\text{O}_2\text{CR})_3$) and tris(trimethylsilyl)phosphine ($\text{P}(\text{SiMe}_3)_3$) to generate the core QDs before shelling with ZnS and ZnSe.^{1,2} While InP QD synthesis has been optimized to the point of commercial production, one of the characteristics that still hinders progress on color purity is the monodispersity of the InP cores. It is now well-known that InP QDs do not proceed through a classical nucleation pathway and instead stray from the La Mer model of nucleation in two ways. The first involves the

intermediacy of atomically-precise magic-sized clusters (MSCs) that have been observed to nucleate, and then fully or partially redissolve before QD growth proceeds.³⁻⁵ This effectively decouples precursor reactivity from the QD growth rate as any changes in reactivity only affect MSC formation. The second important consideration is the observation of a prolonged nucleation period that substantially overlaps with the growth period.⁶ Burst nucleation can no longer be invoked to control monodispersity and instead InP systems are thought to undergo size-focusing growth over long time windows. This limits the accessible size window for which narrow polydispersity can be achieved. With an understanding of these limitations, the isolation and study of InP MSCs have provided new avenues towards controlling the synthesis of InP QD cores with the potential to advance mechanisms for control over QD growth.

The most well-studied InP MSC is $\text{In}_{37}\text{P}_{20}(\text{O}_2\text{CR})_{51}$ which is amenable to gram-scale synthesis and was structurally characterized by single crystal X-ray diffraction (SCXRD) in the case of $\text{R} = \text{CH}_2\text{C}_6\text{H}_5$.⁷ The isolation of $\text{In}_{37}\text{P}_{20}(\text{O}_2\text{CR})_{51}$ led to the development of multiple synthetic routes towards attaining InP QDs with unprecedented characteristics. Hot-injection of the cluster at temperatures greater than 200 °C results in conversion as a single-source precursor producing zinc-blende InP quantum dots.^{3,4} This method was expanded to incorporate Zn^{2+} and Ga^{3+} dopants within the cluster that then allowed for a similar single-source precursor approach towards doped InP QDs.⁸ Both of these conversions were suggested to proceed through cluster dissolution into reactive monomer species, followed by renucleation and subsequent growth of InP QDs. The temperature was found to dictate the quality of the resulting QDs with lower temperatures (<200°C) causing cluster degradation with little to no successive, productive crystal growth. However, at higher reaction temperatures (>200°C) the mechanism of dissolution and subsequent growth resulted in high-quality InP QDs.^{3,4} Beyond hot-injection, the InP cluster has also been documented to template the formation of quasi-wurtzite phase InP QDs. This work represented the first time the phase of the cluster had been documented on that size scale and sets the stage for potential anisotropic InP nanostructure growth.⁹

While these studies are examples of the successful application of InP clusters as isolable single source precursors and seeds for the growth of larger nanostructures, an unresolved question is how it functions in-situ to produce high quality InP QD cores. Multiple studies have documented its presence when synthesizing cores using indium carboxylate and $\text{P}(\text{SiMe}_3)_3$,^{3,5}

and it is thought that dissolution follows in-situ cluster formation, but the extent of dissolution and pathways of regrowth to form high-quality QDs still largely remain a mystery.

Computational studies of $\text{In}_{37}\text{P}_{20}$ have revealed important features that relate its reactivity and structure. Kulik and coworkers developed multiple connections between the carboxylate ligands and the surface reactivity of the InP cluster, leading to the conclusion that the bridging syn-anti binding mode is the most reactive when subjected to P^{3-} .¹⁰ Furthermore, the distance between surface In atoms is the primary descriptor that dictates their susceptibility to displacement by P^{3-} , where longer separations correlate with higher carboxylate dissociation energies. Beyond the study of surface attack driven conversion, *ab initio* molecular dynamics calculations have been performed to better understand the initial mechanistic steps in the thermally induced conversion of clusters.¹¹ Kang and coworkers identified three indium carboxylate units on the cluster surface whose release is what initiates cluster dissolution. Once again, the carboxylate network on the cluster surface is cited as the culprit for directing structural rearrangement.

The structural and reactivity comparisons made by Kang and coworkers also highlight the developing juxtaposition of InP and Cd-chalcogenide clusters. Claims of structural homologies have been made by Robinson and coworkers regarding an α -CdS cluster and the $\text{In}_{37}\text{P}_{20}$ cluster.¹² This spurred two computational studies by Kang and coworkers investigating the possibility of analogous structures in the two materials systems and why InP does not show the bond exchange isomerization under the same conditions that are observed for CdS.^{11,13} Despite these computational efforts, there has yet to be definitive experimental validation of this structural relationship between III-V and II-VI clusters.

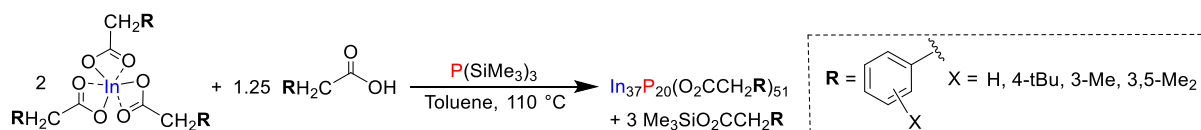
In this work, we sought to experimentally investigate cluster surface chemistry as a powerful leverage point for controlling conversion reactivity and mechanisms. By synthesizing the $\text{In}_{37}\text{P}_{20}(\text{O}_2\text{CR})_{51}$ cluster with a family of substituted phenylacetate ligands possessing differing steric profiles, it is shown that the surface reactivity can be both hindered and accelerated when compared to the parent phenylacetate-ligated cluster. The steric profile is also found to modulate cluster thermolysis reactions by extending nucleation periods at high temperatures (>200 °C), while at lower temperatures (160 °C) the discrete growth of larger molecular intermediates is documented. Furthermore, these studies allowed for the single-crystal

X-ray diffraction study of a smaller member in the InP cluster family that is not only implicated as an intermediate in the reported $P(\text{SiMe}_3)_3$ -induced conversions, but also serves as the first structurally-defined InP homolog to a $\text{Cd}_{14}\text{Se}_{13}$ cluster recently reported by Hyeon and coworkers.¹⁴

Results and Discussion

Structural Characterization

All $\text{In}_{37}\text{P}_{20}(\text{O}_2\text{CR})_{51}$ clusters were synthesized by combining indium carboxylate, carboxylic acid, and $P(\text{SiMe}_3)_3$ according to the previously reported procedure by replacing phenylacetic acid with the same stoichiometry of the substituted phenylacetic acid (**Scheme 1**).⁷ The local environments of the phosphorus atoms within the clusters were probed with ^{31}P NMR spectroscopy (**Figure 1A**). The placement of a *tert*-butyl group in the para-position leads to a similar overall pattern as observed in the case of the parent phenylacetate cluster, but coalescence of signals at -190 ppm and a loss in symmetry evidenced by signal splitting at -235 ppm and -238 ppm is observed in addition to a significant shift in the most downfield resonance at -176 ppm. As steric bulk is increased near the core through meta-substitution, we see significant broadening that makes the assignment of specific P-signals difficult. However, the general shape and range of the ^{31}P resonances remain the same, suggesting that the overall connectivity is preserved. An assignment of the ^{31}P resonances in the parent phenylacetate-ligated cluster spectrum to individual atoms in the crystal structure is provided in the supplemental information (**Figure S1**).



Scheme 1. Synthesis of $\text{In}_{37}\text{P}_{20}(\text{O}_2\text{CCH}_2\text{R})$ clusters with substituted phenylacetate ligands.

These changes in the chemical shift and peak coalescence or splitting indicate internal perturbations in the structure of the $\text{In}_{37}\text{P}_{20}$ cluster that are induced by steric pressure in the ligand sphere. In general, the two factors governing a ^{31}P resonance are the electron density

around the P nucleus and the shielding cones of unsaturated systems.¹⁵ We do not anticipate shielding cones from π -networks making any substantial contribution to the overall resonances given their physical distance from the core P atoms. Furthermore, the aromatic rings in the carboxylate ligands are decoupled from the carboxylate through a CH₂ and all substituents are aliphatic so there should be no significant electronegativity differences between ligands. This leaves the In-P-In bond angles as the primary culprit for controlling and changing the observed resonances. Bond angles impact the resonance by modulating the s-orbital character, with increased s-orbital character resulting in better shielding of the observed nucleus and an upfield shift. For molecular phosphines, a wider Tolman cone angle correlates with more s-orbital character and further upfield resonances.¹⁶ We conclude that the structural modifications induced by the ligand sphere manifest as In-P-In bond angle changes. For instance, the downfield shift observed for the apical phosphorus resonance in the 4-*tert*-butylphenylacetate-ligated cluster is consistent with more acute bonding at that phosphorus atom induced by ligand steric pressure that causes the angles to surface indium atoms to become more acute. Finally, as surface-directed ligand pressure increases, we observe considerable increases in the linewidths of the ³¹P resonances. This trend can be interpreted through the lens of the characterization of proteins using NMR spectroscopy where structural rigidity can be correlated with linewidth.¹⁷ We believe that the meta-substituents greatly enhance the rigidity of the surface indium carboxylate through hindered ligand rotation, thereby interfering with the nuclear relaxation rate which is known to vary inversely with molecular mobility. These broadened resonances then suggest that the meta-substituents hinder the structural flexibility leading to a more rigid cluster structure.

The structure of the In₃₇P₂₀ cores were investigated with X-ray pair distribution function (PDF) analysis (**Figure 1B**).¹⁸ The reduced PDF, $G(r)$, reveals only minor structural differences between ligand substituents, confirming that the core In₃₇P₂₀ stoichiometry and connectivity is left unchanged on average. Nearest neighbor peaks in $G(r)$ represent In-O, and In-P pairs at distances of 2.19 Å and 2.53 Å respectively (**Figure S2, S3**).⁷ The second-nearest neighbor peak at 4.15 Å and the peaks beyond predominantly display In-In distances due to stronger X-ray scattering by this atom pair. Compared to peak positions of the phenylacetate-ligated cluster, $G(r)$ peaks of the other ligand substituents generally exhibit small shifts to shorter distances in real space. The largest shifts are observed for the 4-tBu substituent, where In-O (2.17 Å) and In-P (2.51 Å) peak positions equate to an average compressive strain of 0.9% compared to

phenylacetate. Changes in peak shape and position are also evident at longer correlation distances (≥ 10 Å) that approach the overall particle diameter, which suggest variability in surface In geometries and are further indicators of compressive strain imposed on the InP cluster (Figure S4).

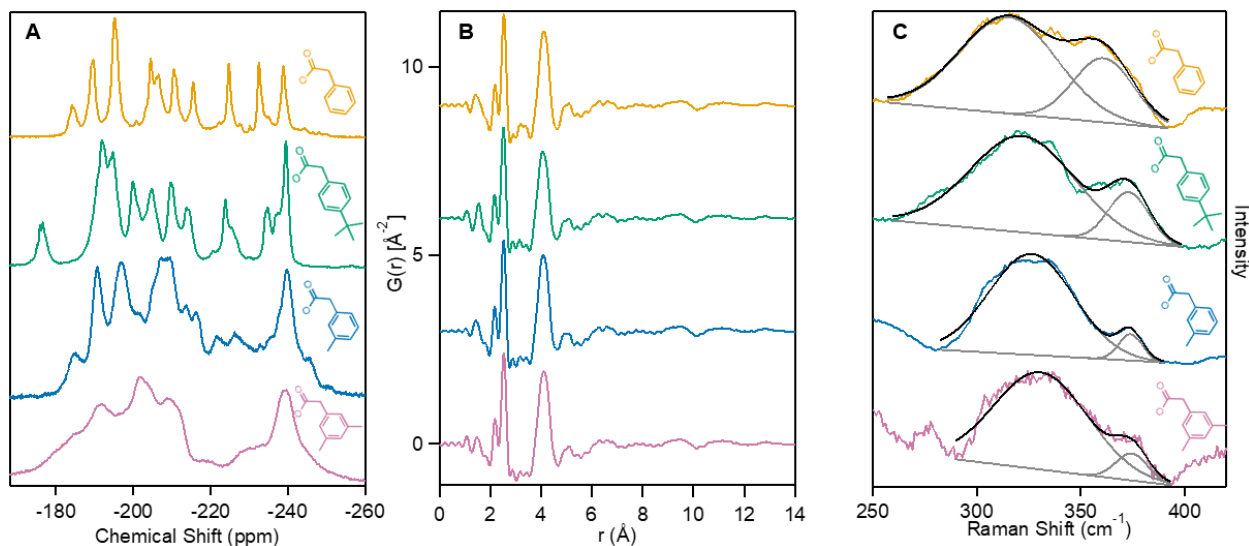


Figure 1. A) ^{31}P NMR spectra of phenylacetate-ligated $\text{In}_{37}\text{P}_{20}$ clusters with H, 4-tBu, 3-Me, and 3,5-Me₂ substituents. B) Pair distribution function for all clusters from X-ray total scattering (offset for clarity). C) Raman spectra for all clusters using $\lambda_{\text{exc}} = 785$ nm. The 290-390 cm^{-1} region was fit to two Gaussian distributions representing two collections of vibrations involving In and P atoms.

The isolated and purified clusters were further characterized by Raman spectroscopy to investigate ensemble behavior arising from ligand-induced structural perturbations. Previous characterization of myristate-ligated InP clusters has approximated the Raman signal from the clusters as two separate vibrational modes centered at 320 cm^{-1} and 365 cm^{-1} .⁹ These vibrations are distinct from the transverse and longitudinal optical modes (TO and LO) at 306 and 348 cm^{-1} respectively, reported for bulk zinc-blende InP.¹⁹ On the nanoscale, both the TO and LO phonons are distinct and represented in InP QDs with the relative TO peak intensity increasing with smaller QDs and the LO-TO peak separation increasing with increasing QD size.^{20,21} These trends do not extend into the InP cluster regime as the quasi-wurtzite phase is cluster specific and has an entirely different atomic arrangement compared to the common zinc-blende QDs. This

leads to a distinct spectrum of InP-based Raman-active vibrations in clusters that can be approximately fit by two gaussians representing a low frequency region and a high frequency region (**Figure 1C and Figure S5**). A similar spectral shape has been reported in the Raman spectra of atomically precise CdSe clusters, with the lower and higher frequencies attributed to surface and interior modes, respectively.²² For the phenylacetate-ligated cluster, these regions are centered at 315 cm⁻¹ and 361 cm⁻¹. With steric pressure increasing from 4-tBu to 3-Me and 3,5-Me₂, the low frequency center shifts to 322 cm⁻¹, 326 cm⁻¹, and 330 cm⁻¹ respectively (**Table S1**). A similar but reduced trend is seen with the high frequency region shifting to 373 cm⁻¹, 374 cm⁻¹, and 375 cm⁻¹. Comparing the relative integration of low and high frequency regions between clusters shows 70% and 30% contributions from each respective region for phenylacetate, 80% and 20% for 4-tBu, and finally 90% and 10% for both 3-Me and 3,5-Me₂. This behavior is reminiscent of reported phonon mode modulation in graphene through pressure-induced strain.^{23–25} In these reports, the induced strain results in a shift to lower frequency of Raman-active phonon modes. Similar softening behavior of vibrations that contribute to the high frequency region would produce a shift in the center of both high and low frequency regions to higher wavenumber. This would then be coupled with an increase in the overall signal at low frequency that is compensated for by a decrease in the signal at higher frequency. These phenomena are indeed experimentally observed as described above. This corroborates the trend observed in the ³¹P NMR linewidths and suggests the rigidity of the meta-substituted ligand sphere is imparting strain on the interior of the cluster, causing modulation of the Raman-active InP-based vibrational modes. .

While the vibrations of the cluster core can be observed in the Raman spectra, the ligands can be more readily analyzed with FTIR spectroscopy. The ability to approximate carboxylate binding mode populations on the InP cluster surface has been developed previously.^{26,27} The single crystal structural characterization and subsequent IR studies of molecular zinc carboxylate complexes has allowed for the determination of binding mode-dependent symmetric and asymmetric carboxylate stretch frequencies as $\Delta\omega = \omega_{\text{asymmetric}} - \omega_{\text{symmetric}}$.²⁸ These can be applied to indium carboxylates on the surface of the cluster to follow the general order: $\Delta\omega_{\text{chelating}} < \Delta\omega_{\text{bridging (syn-anti)}} < \Delta\omega_{\text{bridging (syn-syn)}} < \Delta\omega_{\text{monodentate}}$. Using this approach to approximate the relative binding mode populations on the InP cluster surface showed that, in solution, the bridging (syn-anti) is the predominant configuration followed by bridging (syn-syn) and finally, chelating and

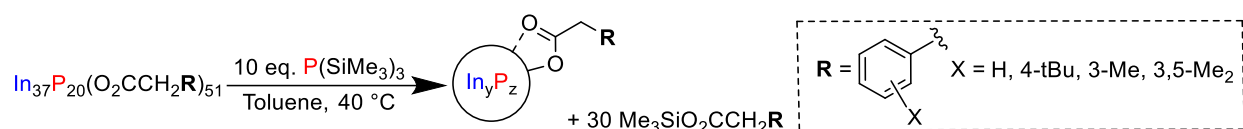
monodentate.²⁶ This approach was implemented in this study to observe approximate distributions of particular binding motifs and any correlations with the ligand steric profile in solution. Between the phenylacetate-ligated cluster and its meta-substituted derivatives, there appears to be little difference in populations across all binding modes. The bridging modes make up the majority of passivation with some minor contributions from the chelating and monodentate binding modes. With the addition of the *tert*-butyl substituent, the relative contribution from the chelating and monodentate binding modes increase by 3% and 5% respectively compared to the phenylacetate. These increases are compensated for by a decrease in both bridging populations. Considering a 2% increase approximates a difference of one ligand changing its coordination on the surface, these percentages suggest, at most, a two-ligand binding conformation change in solution (**Figure S6, S7**). Furthermore, we acknowledge the inherent uncertainty in a 4 gaussian fit to a narrow wavenumber range with little peak definition. Overall, the solution-phase FTIR serves to indicate that the binding mode distributions are remarkably similar, if not identical, across different degrees of ligand steric profiles.

Conversion and Reactivity

After characterizing the ligand-induced structural perturbations, we turned to testing the reactivity of all clusters. It is worth noting at this point that we also explored the synthesis of *o*-tolylacetate and 3,5-di-*tert*-butylphenylacetate-ligated clusters providing early clues about reactivity differences as a function of ligand steric profile. With *o*-tolylacetate, the cluster transiently formed and could be characterized by UV-Vis but over the course of a few hours destabilized into smaller, insoluble species (**Figure S8**). Using 3,5-di-*tert*-butylphenylacetic acid in the reaction may have formed the cluster, but it was quickly bypassed before spectroscopic characterization could confirm the presence of cluster, forming larger quantum dots and thus again, the cluster was not stable enough to be isolated (**Figure S9**).

Previously our group has shown that further addition of P(SiMe₃)₃ induces partial fragmentation of the InP cluster followed by templated growth of quasi-wurtzite QDs.⁹ This is initiated by P(SiMe₃)₃ reacting with indium-bound carboxylates to liberate silyl ester with formation of a new In-P bond. Through the sequential removal of carboxylates, the cluster eventually fragments forming a higher symmetry core intermediate along with the liberation of InP monomer species. The monomers then add back to the core forming larger nanocrystals.

Computational work from Kulik and coworkers has suggested that a vital parameter governing the ease of carboxylate displacement by P^{3-} is the In-In separation distance.¹⁰ Furthermore, as a part of the same study, a computational comparison between phenylacetate and acetate-ligated InP clusters suggested that π - π stacking between adjacent phenyl groups can create negative deviations in In-O dissociation energies. While the ring is decoupled from the carboxylate by the methylene group, there is still an electronic effect from the ring that can be augmented by π - π stacking. We hypothesized that the variations in steric profile and substitution of the phenyl ring could modulate surface indium separation and direct surface π - π stacking thereby tuning the susceptibility of carboxylate displacement by $P(SiMe_3)_3$.



Scheme 2. Formation of quasi-wurtzite phase InP nanocrystals through the addition of $P(SiMe_3)_3$ to $In_{37}P_{20}(O_2CCH_2R)_{51}$ clusters.

To observe the kinetics of conversion, a solution containing 10 equivalents of $P(SiMe_3)_3$ was injected into a solution of cluster in toluene at 40 °C (**Scheme 2**). The rate of growth was then measured by tracking absorbance changes over time with the 3-Me cluster conversion shown as an example in **Figure 2A**. Conversion plots for all clusters can be found in **Figure S10**. The change in absorbance at 500 nm over time is shown in **Figure 2B**. Monitoring the conversion at other wavelengths shows the same trend and can be found as **Figure S11 and Table S2**. The inflection point for growth was found through the maximum of the first derivative and the progression of the reaction up to this point we refer to as the induction period (**Figure S12**). The reaction beyond the inflection point is referred to as the growth region. Fitting the growth region of these traces to a single exponential allows for an approximate k_{obs} value to be extracted from each conversion reaction. With fitting across multiple wavelengths, the induction period from shortest to longest follows the order 3,5-Me₂ (31.3 ± 1.2 min), H (41.0 ± 2.0 min), 3-Me (42.7 ± 1.2 min), and 4-tBu (89.0 ± 20.6 min). Across the same wavelengths, the growth rate from fastest to slowest is 3,5-Me₂ (0.048 ± 0.001), 3-Me (0.035 ± 0.002), H (0.028 ± 0.004) and 4-tBu (0.014 ± 0.002) (**Figure 2C, Table S2, Figure S13, S14**). The phenylacetate-ligated

cluster conversion products aggregate and begin to lose colloidal stability at the 82nd minute due to less favorable solvent-ligand interactions leading to a linear region in the absorbance vs time plots. This region was excluded when calculating k_{obs} from the growth region for the phenylacetate cluster. These trends clearly show a substantial increase in reactivity from the 4-tBu substituted cluster to the 3,5-Me₂ cluster. A direct comparison of the phenylacetate and 3-Me ligands shows that while the induction periods are nearly identical, the growth rates are different. We rationalize this by introducing two processes that make up the induction period, diffusion and displacement. The addition of a methyl group hinders the diffusion of P(SiMe₃)₃ through the ligand shell to the cluster surface but simultaneously augments the reactivity of In-O bonds. The balance between hindering diffusion and augmenting reactivity is what determines the induction period. This is why the phenylacetate-ligated cluster may begin liberating monomer at a similar time as the 3-Me cluster but overall has a slower growth rate. In the case of 3,5-Me₂, the drastic increase in the reactivity of the surface more than compensates for any restricted diffusion giving it the shortest induction period and highest reactivity. For 4-tBu, the steric profile leads to a vastly slower diffusion rate which dominates the slower reactivity of the cluster. We have also confirmed by *in-situ* solution-phase FTIR that the bridging syn-anti carboxylate binding sites are indeed the most reactive on the cluster being selectively displaced by P(SiMe₃)₃ to induce fragmentation (**Figure S8**).

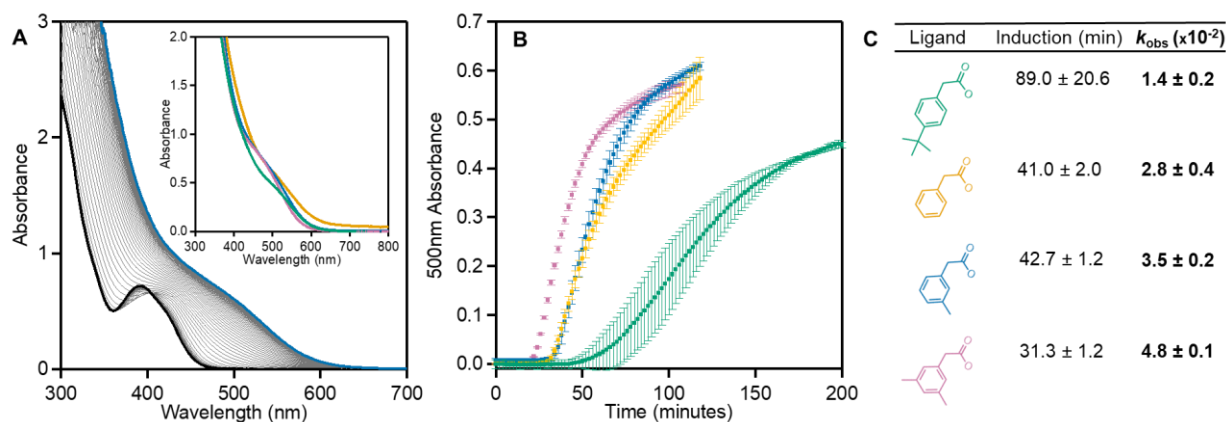


Figure 2. A) Example conversion of 3-Me In₃₇P₂₀ cluster into InP nanocrystals over 118 minutes through P(SiMe₃)₃ addition. The inset shows the final absorbance profile for each ligand averaged across 3 trials. B) Absorbance at 500 nm over time after the addition of 10 eq. of

P(SiMe₃)₃ to each cluster. C) Induction time and k_{obs} as measured from the 500 nm absorbance trajectory and fit to a single exponential.

This pattern of reactivity shows that both the placement and extent of substitution are important factors in engineering the surface for controlling reactivity. With meta-substituents directed at one another, steric crowding on the surface could force bridging carboxylates to shorten In-In separation distances thereby increasing the reactivity (**Figure 3A**) as predicted by the computational model from Kulik and coworkers. The bulky para-substituent greatly hinders reactivity by slowing phosphine ingress (**Figure 3B**). Furthermore, the meta-substituted phenyl groups could also selectively organize with π - π stacking to minimize the steric pressure from adjacent substituents (**Figure 3C**). These three processes likely occur constructively with all ligands to determine the overall reactivity.

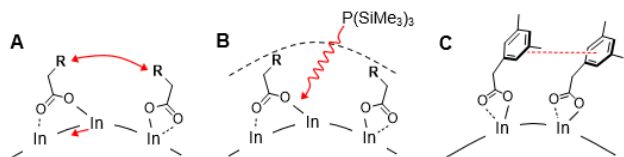


Figure 3. A) Steric pressure between ligands shortens indium separation distances to enhance reactivity. B) A larger steric profile discourages P(SiMe₃)₃ diffusion to the cluster surface to decrease reactivity C) Meta-substituents direct the alignment of π - π stacking to favor ligand dissociation and enhance reactivity.

The reactivity differences between these clusters were also tested by thermolysis. As mentioned above, it is thought that thermally induced InP cluster to QD conversion above 200 °C proceeds through complete dissolution and renucleation of QDs. For these hot-injection studies using the clusters as single-source precursors, it is unlikely that the thermally induced conversions will have much dependence on surface reactivity. The dissolution of cluster into monomers at these temperatures likely does not involve any appreciable amount of surface attack as there is no secondary species to induce destabilization. Instead, the cluster dissolution is likely brought on by thermally instigated bond vibrations exceeding a critical distortion similar to the

Lindemann melting criterion.²⁹ The conversion of clusters with different ligands to QDs through this mechanism is then dependent upon two factors: the thermal stability of the cluster and the steric profile of the ligand. Monitoring the change in absorbance at 500 nm throughout the hot-injection reactions suggests that the conversion of these clusters at 240 °C is very much ligand dependent. With less bulky substituents, H and 3-Me, there is a significant degree of QD growth shown by an increase in absorbance at 500 nm within 3 minutes of the injection. This is accompanied by a disappearance of the cluster absorbance feature at 386 nm. Comparatively, the bulkier substituents, 3,5-Me₂ and tBu, show less development at 500 nm during early time points suggesting a slower growth rate (**Figure 4A, Figure S15, S16**). There is not a profound difference in the persistence of the 386 nm feature with bulkier substituents suggesting that the monomer production rate across different ligands is similar. These conversions result in the final absorbance traces shown in **Figure 4B** which demonstrate that the initial rate of growth can be correlated with the λ_{max} of the final QDs where bulkier substituents converge on a shorter λ_{max} (**Figure S17, Table S3**). The size trend observed in the absorbance was corroborated by TEM (**Figure S18, Table S4**). Many previous studies have documented the correlation between carboxylate chain length and resulting size of nanocrystals where longer chain lengths direct smaller QDs.^{30–32} These results were rationalized by asserting that longer fatty acid chains slow nucleation and growth. This interpretation was reinvestigated by De Nolf et al. to determine that the size control with long chain fatty acids can also be explained by chain length changing the rate of diffusion as well as the solubility of the monomer species during nucleation and growth.³³ Using these studies as a framework to interpret our observed size-dependence provides three possible rationales. Firstly, aligned with the study of De Nolf et al., there could be a difference in the diffusion and solubility of monomer species generated from cluster dissolution. Secondly, the substitution of the phenyl group could direct different degrees of surface tension from interligand interactions. Finally, the ligand steric profile may impact the kinetic balance between nucleation and growth leading to different sizes. Now addressing these interpretations, we do not anticipate any impactful differences in diffusion and solubility between ligands. Especially using 3-Me and 3,5-Me₂ as points of comparison, the addition of a single methyl group should not substantially affect diffusion or solubility to generate a size difference of this magnitude. While we do anticipate differences in surface tension across the suite of ligands, the observable size trend does not follow what we would predict to be the trend in surface tension. Seeing that meta-

substituents greatly enhance the rigidity of the cluster surface, it would follow that the 3-Me and 3,5-Me₂ ligated QDs should have the highest surface tension which should correlate with larger nanocrystals but this trend is not experimentally observed. Finally, the relationship can be rationalized by the steric profile altering the balance between nucleation and growth after cluster dissolution. A larger steric profile of monomer species and nanocrystal surface should reasonably hinder growth thereby maintaining a high monomer concentration for longer time periods. Considering higher monomer concentrations favor nucleation overgrowth, steric hindrance restricting growth should benefit the production of nuclei resulting in a larger number of nuclei and a smaller average particle radius. This rationale fits the observed experimental trend so while diffusion, solubility and surface tension may contribute to the size trend, we conclude that the mechanism of In₃₇P₂₀ thermolysis is dominated by restricted surface growth.

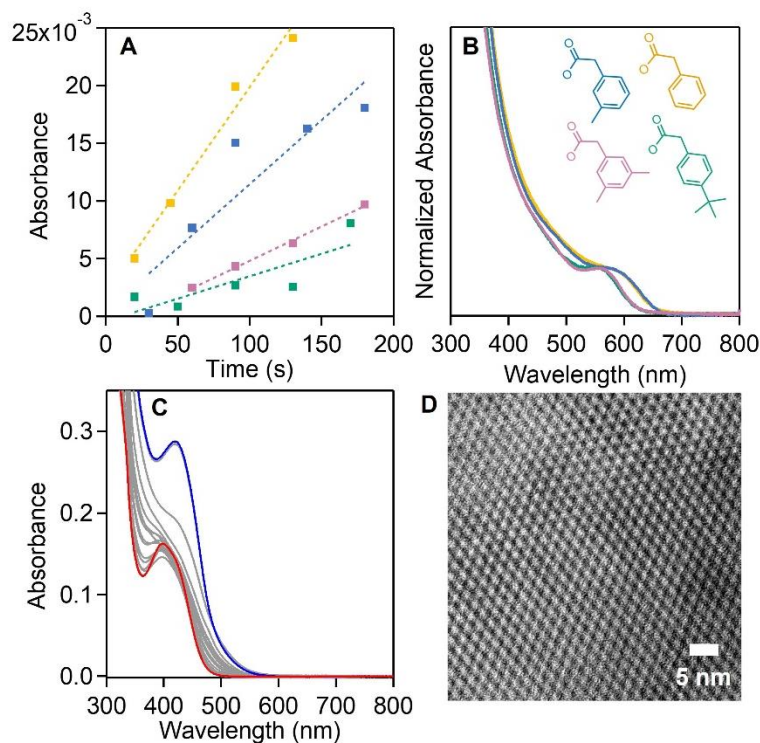


Figure 4. A) Dependence of QD growth rate on ligand substitution by monitoring the change in absorbance at 500 nm over early time points. H (yellow), 4-tBu (green), 3-Me (blue), and 3,5-Me₂ (pink). The dotted lines are linear best fits but serve to primarily guide the eye. B) Absorbance of final QDs after complete conversion synthesized from thermolysis of clusters at

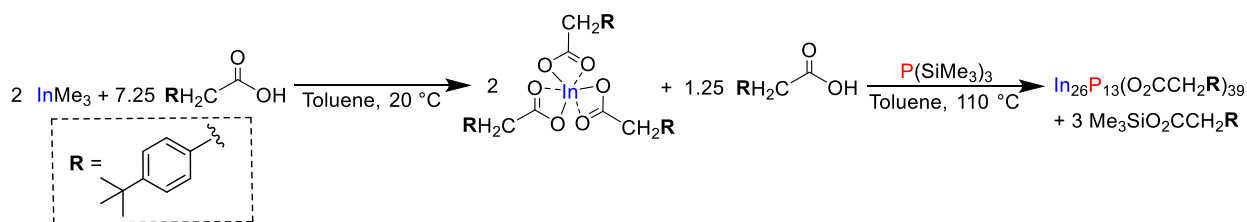
240 °C for 120 min. C) Conversion of 3-Me cluster to InP-419 at 160 °C from 0 min (red) to 20 hrs (blue). D) TEM of InP-419 formed from 3-Me cluster conversion.

Similar conversion studies through thermolysis of myristate-ligated $\text{In}_{37}\text{P}_{20}$ clusters showed that little productive nucleation occurs at 150 °C.⁴ Instead, the cluster follows a dominant decomposition route resulting in poorly defined, agglomerated InP species. Interestingly, this decomposition route is not observed with the family of phenylacetate-ligated InP clusters when undergoing thermolysis at 160 °C in mesitylene. Instead, over the course of 22 hours, we see the conversion of the $\text{In}_{37}\text{P}_{20}$ species into a new species with a well-defined absorbance centered at 419 nm (InP-419, **Figure 4C**). Not only does this species show the same quasi-wurtzite phase of the parent $\text{In}_{37}\text{P}_{20}$ cluster by powder XRD (**Figure S19**) but can also be arranged into an extensive superlattice indicating an extremely high degree of monodispersity and the potential for a molecularly defined species (**Figure 4D, S20**). While the progression from $\text{In}_{37}\text{P}_{20}$ towards InP-419 is documented for the phenylacetate, tBu, and 3-Me clusters, the yield of this material is highest with the 3-Me cluster suggesting that the degree of rigidity that this substituent provides helps to stabilize the surface through this conversion (**Figure S21**). This thermally induced conversion resulting in a substantial red-shift, quasi-wurtzite XRD pattern, and high degree of monodispersity is reminiscent of the computational study from Kang and coworkers investigating the formation of the $\beta\text{-In}_{34}\text{P}_{20}$ cluster isomer.¹¹ They found that through thermolysis, the isomerization was instigated by the loss of three indium carboxylate units from the cluster surface. It is likely that a similar process is occurring in these experimental reactions where prolonged heating near the point of thermal stability causes the $\text{In}_{37}\text{P}_{20}$ cluster to liberate some number of surface indium carboxylates leading to a structural reorganization to InP-419. While the characterization of differences in structure and stoichiometry between $\text{In}_{37}\text{P}_{20}$ and InP-419 are dependent upon SCXRD, these lower temperature conversions expand the reaction landscape of InP clusters and provide additional detail on the mechanism of dissolution of InP clusters on the path to QDs.

In₂₆P₁₃ Synthesis and Characterization

After tracking and characterizing the ligand-dependent cluster conversions both through thermolysis and $\text{P}(\text{SiMe}_3)_3$ addition, we sought to further explore the implications of the hindered

precursor diffusion that the tBu group provides. While investigating the routes toward generating the indium carboxylate, we found that when neatly reacting the 4-*tert*-butylphenylacetic acid with indium acetate to form the indium carboxylate precursor in an In₃₇P₂₀ cluster synthesis, the result is a partially soluble indium precursor. However, when the indium carboxylate is made through the reaction between trimethylindium and 4-*tert*-butylphenylacetic acid, the resulting precursor is completely soluble in toluene at room temperature. Using the indium carboxylate made through trimethylindium in the cluster synthesis leads to a new species absorbing at 350 nm, indicative of a smaller cluster (InP-350, **Scheme 3, Figure 5A.**). Using any of the other carboxylic acids and trimethylindium to generate the indium carboxylate did not result in the same 350 nm absorption when reacted with P(SiMe₃)₃. Instead, the 386 nm absorbance of the In₃₇P₂₀ cluster is observed. We therefore hypothesize that it is the tBu group hindering the diffusion of P(SiMe₃)₃ to react with surface carboxylates that causes this difference in cluster formation. Slowing diffusion and protecting the surface significantly decreases the rate of cluster growth in favor of P(SiMe₃)₃ reacting with unincorporated, molecular indium carboxylate. This leads to the complete consumption of the phosphine before the In₃₇P₂₀ cluster has formed. Therefore, we have kinetically trapped a smaller cluster that is along the reaction pathway to form In₃₇P₂₀ by controlling the rate of diffusion to the cluster surface. The neat reaction between indium acetate and 4-*tert*-butylphenylacetic acid generating a precursor that directly forms In₃₇P₂₀ is likely due to incomplete conversion of indium acetate to indium 4-*tert*-butylphenylacetate. This leaves a larger excess of unreacted free acid that enhances the reactivity of the P(SiMe₃)₃ by formation of HP(SiMe₃)₂, H₂P(SiMe₃) and H₃P.



Scheme 3. Synthesis of cluster fragment leveraging the enhanced stability of the 4-tBu substituent.

The previous study done by our group investigating the reaction between $\text{In}_{37}\text{P}_{20}$ and $\text{P}(\text{SiMe}_3)_3$ found that the addition of 1-2 equivalents of $\text{P}(\text{SiMe}_3)_3$ with respect to cluster led to just fragmentation and no subsequent growth.⁹ Under these conditions, the fragmentation resulted in a new molecular structure that could only be characterized by UV-Vis and ^{31}P -NMR spectroscopy. In particular, the ^{31}P -NMR spectrum showed four sharp resonances in the -195 to -230 ppm region. Further investigation showed that the smaller structure could be synthesized bottom-up but only in small quantities and was not stable enough for isolation. Interestingly, characterizing the new cluster made through 4-*tert*-butylphenylacetic acid absorbing at 350 nm with ^{31}P -NMR showed the same four sharp resonances previously documented (**Figure 5B**). Seeing that near stoichiometric equivalents of $\text{P}(\text{SiMe}_3)_3$ leads to fragmentation into the smaller cluster and any further amounts of phosphine result in templated growth, we hypothesize that this smaller cluster functions as an intermediate in the $\text{P}(\text{SiMe}_3)_3$ -induced conversion mechanism. Furthermore, previous work has shown the final product to be temperature dependent but completely independent of cluster concentration.⁹ This is further evidence for a reaction mechanism that proceeds by conversion through this intermediate.

The rigidity of the *tert*-butyl group not only stabilized the cluster and modulated diffusion of $\text{P}(\text{SiMe}_3)_3$ but also allowed for growth of X-ray quality single-crystals and full structural determination (**Table S5**). This revealed the intermediate to have the formula $\text{In}_{26}\text{P}_{13}(\text{O}_2\text{CR})_{39}$ (**Figure 5C**). In previous work our group had provided an initial guess of the composition of this intermediate as $\text{In}_{29}\text{P}_{14}(\text{O}_2\text{CR})_{45}$.⁹ This initial hypothesis was very close to the true identity but assumed that the fragment would be a symmetric subset of the original $\text{In}_{37}\text{P}_{20}$ species maintaining the central indium.

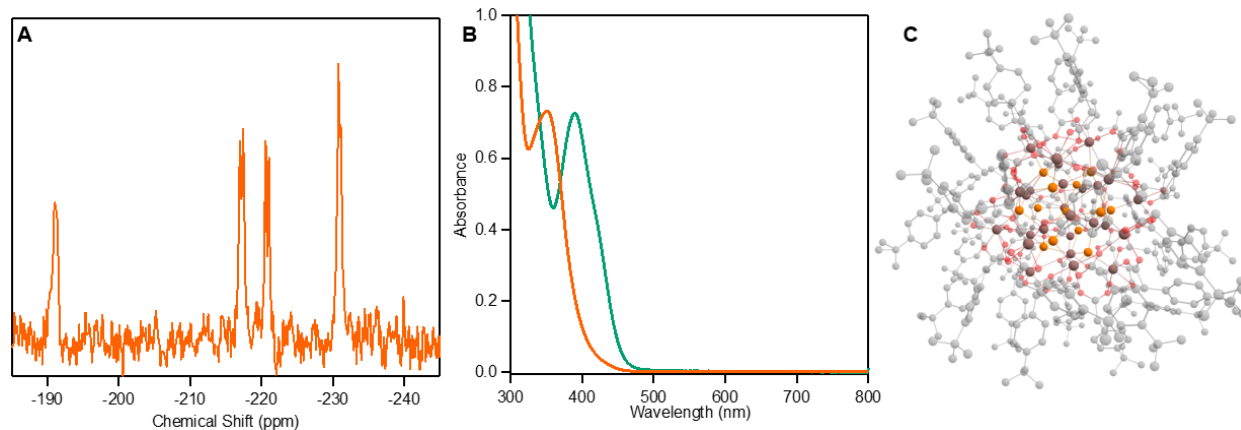


Figure 5. A) ^{31}P NMR spectrum of $\text{In}_{26}\text{P}_{13}(\text{O}_2\text{CCH}_2\text{C}_6\text{H}_4\text{-tBu})_{39}$ cluster fragment. B) Absorbance comparison between isolated $\text{In}_{26}\text{P}_{13}$ cluster (orange) showing a λ_{max} at 350 nm and isolated $\text{In}_{37}\text{P}_{20}$ cluster (green) showing a λ_{max} at 386 nm. C) Single-crystal XRD structure of $\text{In}_{26}\text{P}_{13}(\text{O}_2\text{CCH}_2\text{C}_6\text{H}_4\text{-tBu})_{39}$ with hydrogen atoms removed for clarity.

The structure was elucidated to be a higher-symmetry fragment of the $\text{In}_{37}\text{P}_{20}$ cluster with a central P atom. Structural overlay shows that the root mean squared deviation between paired atoms in $\text{In}_{26}\text{P}_{13}$ vs $\text{In}_{37}\text{P}_{20}$ is 0.438 Å, which emphasizes the strong similarities between these two structures (**Figure S22**). Even the dangling surface In atoms are positioned as they would be for integration into the cluster core upon growth. The five ligand binding modes, monodentate, chelating, bidentate dative, symmetric bridging, and asymmetric bridging, represented on the surface of the $\text{In}_{37}\text{P}_{20}$ cluster are all also represented on the surface of $\text{In}_{26}\text{P}_{13}$ but with a different distribution. Of the 39 carboxylates, 7 are chelating, 5 are bidentate dative, 10 are symmetric bridging, 16 are asymmetric bridging, and 1 is forced into a monodentate configuration by a bound water molecule. Trace water from polar solvents used in crystallization were found to bind readily to the surface of the cluster similar to the previously reported $\text{In}_{37}\text{P}_{20}(\text{O}_2\text{CR})_{51}(\text{H}_2\text{O})$ structure that was generated when the original InP cluster was exposed to humid conditions.⁷ The average In-In separation distance in bridging carboxylates for the $\text{In}_{37}\text{P}_{20}$ cluster is found to be 4.75 Å. For $\text{In}_{26}\text{P}_{13}$ this metric was determined to be 4.46 Å. The decrease in In-In separation distance suggests a more reactive surface as predicted by Kulik and coworkers and reinforces the trend of surface In separation increasing from early-stage clusters to quantum dots.¹⁰ In the case of $\text{In}_{37}\text{P}_{20}(\text{O}_2\text{CR})_{51}(\text{H}_2\text{O})$, water is found to displace a chelating ligand thereby forcing it to adopt a monodentate configuration. This occurs selectively on an indium passivating the apical phosphorus atom of the cluster. Despite the local ligand rearrangement, the bound H_2O is found to have negligible effect on the average In-In separation distances (also found to be 4.75 Å) and binding mode populations which remain unchanged hold the displaced chelating carboxylate. This is true even for the In-In separation distances directly involving the In that binds the H_2O . Finally, the four ^{31}P resonances in the NMR spectrum can be assigned to environments in the crystal structure where the three most downfield signals are the sets of four P atoms that

superimpose under each of the three C_2 axes and the final most upfield environment being the center P atom (**Figure 5**).

Analyzing the $[\text{In}_{14}\text{P}_{13}]^{3+}$ core of the $\text{In}_{26}\text{P}_{13}$ cluster reveals T point group symmetry (**Figure 6**). Furthermore, with the surface In atoms removed, the $[\text{In}_{14}\text{P}_{13}]^{3+}$ core is structurally homologous to the TMEDA and Cl ligated $\text{Cd}_{14}\text{Se}_{13}$ reported by Hyeon and coworkers.¹⁴ This is strong evidence for the similarities in structure between the many reported II-VI MSCs and the carboxylate-ligated III-V clusters. The comparative cation-richness of the InP is derived from the requirement for complete 4-coordination of P atoms, which is behavior not seen with analogous CdSe structures. Computational comparisons between III-V and II-VI nanomaterials show that with CdSe, the Se atoms can exist as 2-coordinate without restructuring whereas with InP materials, the P atoms almost exclusively exist as 3- or 4-coordinate.³⁴ Within the $\text{Cd}_{14}\text{Se}_{13}$ cluster, all Se atoms are 3-coordinate except for the central, 4-coordinate atom. This relaxed requirement for chalcogen passivation drives the wider horizon of stoichiometries documented in II-VI materials whereas the 4-coordinate requirement of InP restricts the known cluster stoichiometries to being cation rich. These structural comparisons can be extended further to the observed conversion of $\text{Cd}_{14}\text{Se}_{13}$ to CdSe-420 whose structure lacks full determination but it has been posited that the underlying geometry of CdSe-420 is homologous to that of the $\text{In}_{37}\text{P}_{20}$ cluster with minor differences in stoichiometry.^{14,35} The recently reported structure of $\text{Cd}_{26}\text{Se}_{17}$ synthesized through the cation exchange of $\text{Cu}_{26}\text{Se}_{13}$ furthers this analysis.^{36,37} Both of these clusters show the same general anion sublattice as the $\text{In}_{26}\text{P}_{13}$ cluster and by extension, $\text{In}_{37}\text{P}_{20}$ and $\text{Cd}_{14}\text{Se}_{13}$. It is noteworthy that the growth of the anion sublattice that occurs from $\text{Cu}_{26}\text{Se}_{13}$ to $\text{Cd}_{26}\text{Se}_{17}$ does not follow the same progression of growth as $\text{In}_{26}\text{P}_{13}$ to $\text{In}_{37}\text{P}_{20}$ despite the same initial sublattice structure. $\text{In}_{26}\text{P}_{13}$ requires asymmetric growth off of one side of the cluster to form the $\text{In}_{37}\text{P}_{20}$ structure. In comparison, the 4 Se atoms that are added upon cation exchange all grow off of geometrically equivalent sites. These structural differences between the III-V and II-VI materials could potentially be derived from the difference in ligand type where the mixed environment of L-type phosphines and X-type iodides of the $\text{Cd}_{26}\text{Se}_{17}$ direct a more stoichiometric ratio compared to the only X-type carboxylates of the InP-based clusters.

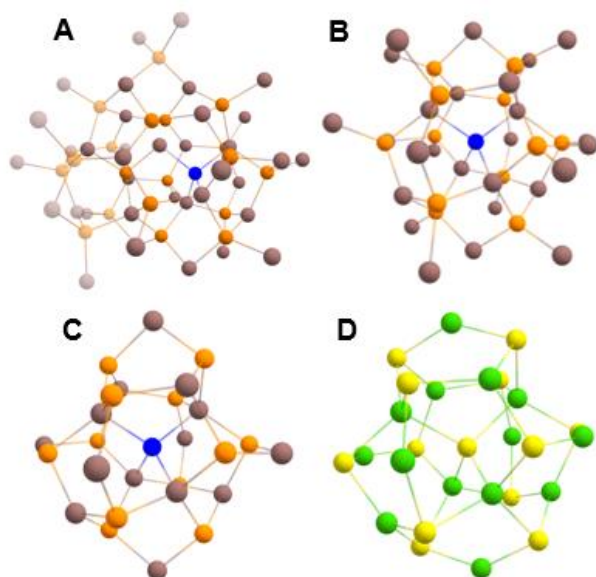


Figure 6. Structural comparisons of $\text{In}_{37}\text{P}_{20}$, $\text{In}_{26}\text{P}_{13}$, and $\text{Cd}_{14}\text{Se}_{13}$. The central P atom of the $\text{In}_{26}\text{P}_{13}$ cluster is highlighted in blue for clarity. A) Crystal model of $\text{In}_{37}\text{P}_{20}$ showing the sub-portion that makes up the $\text{In}_{26}\text{P}_{13}$ cluster (non-transparent). B) $\text{In}_{26}\text{P}_{13}(\text{O}_2\text{CCH}_2\text{C}_6\text{H}_4\text{-tBu})_{39}$ with all carboxylate ligands removed. C) $[\text{In}_{14}\text{P}_{13}]^{3+}$ core presenting T-symmetry and structural analogy to $[\text{Cd}_{14}\text{Se}_{13}]^{2+}$ core. D) Structure of $[\text{Cd}_{14}\text{Se}_{13}]^{2+}$ core without ligands.¹⁴ removed.

To further investigate the electronic structure of $\text{In}_{26}\text{P}_{13}$, we performed TDDFT calculations using TD-HSE06/LANL2DZ. The predicted energies of the first transitions show good agreement with the experimentally acquired spectrum (**Figure 7A**). Analyzing the leaving and arriving orbitals shows that the electronic ground state is essentially entirely composed of phosphorus 3p orbitals (**Figure 7B**). The arriving orbital shows a significant degree of delocalization across the cluster and is primarily composed of phosphorus 4s and indium 5s orbitals (**Figure 7C**). This stands as an interesting comparison with the arriving orbital of $\text{In}_{37}\text{P}_{20}$ which shows a much larger degree of localization and a smaller contribution from indium 5s to make up the NTO. The five discrete transitions that make up the overall peak shape arise from leaving orbitals that are all some arrangement of electron density distributed across different localized phosphorus 3p orbitals (**Figure S23, S24**). This causes the leaving orbitals of the five lowest energy transitions to be very close to degenerate. Furthermore, these transitions all have the same arrival orbital which is isolated energetically from the next two higher energy arriving

orbitals. Both of these higher energy arriving orbitals show much larger degrees of surface localization which result in higher relative energies. Simulated Raman modes of $\text{In}_{26}\text{P}_{13}$ match well with those computed and measured for $\text{In}_{37}\text{P}_{20}$ (**Figure S25**).

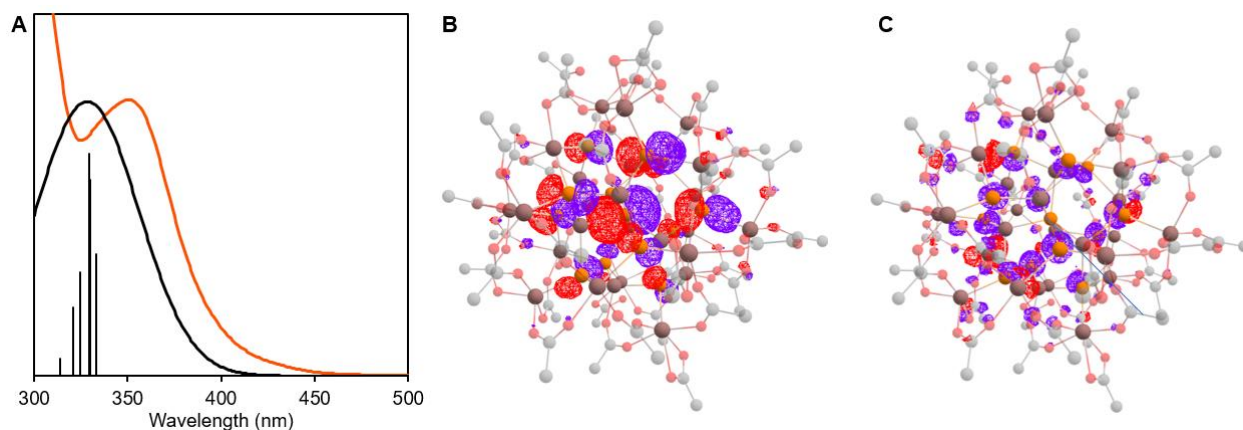


Figure 7. A) Experimental absorption of $\text{In}_{26}\text{P}_{13}$ (orange) compared to the first 5 electronic transitions as predicted by TDHSE06/LANDL2DZ (grey). B) Visualization of the leaving NTO of the lowest energy transition. C) Visualization of the arriving NTO of the lowest energy transition. NTOs were plotted with an isosurface value of 0.025.

Conclusions

The addition of sterically hindered phenylacetate ligands to the surface of $\text{In}_{37}\text{P}_{20}$ clusters modifies the local structural environment of phosphorus atoms without a change in atomic connectivity as evidenced by ^{31}P -NMR spectroscopy and PDF analysis. The addition of para and meta-alkyl substituents to the phenylacetate ligand shell also dampen Raman-active InP-ensemble vibrations through straining surface indium carboxylates. We were also able to identify the substituent extremes that do not allow for cluster isolation in the form of *o*-tolylacetate and 3,5-di-*tert*-butylphenylacetate.

We have further shown that the surface reactivity of $\text{In}_{37}\text{P}_{20}$ clusters can be modulated by the steric profile of the phenylacetate-derived ligands. Steric substitution in the para-position was observed to protect the surface against $\text{P}(\text{SiMe}_3)_3$ attack thereby reducing the rate of conversion to QDs. In contrast, meta-positioned substituents enhanced the reactivity by shortening the separation distance between surface indium atoms and directing π - π stacking among ligand

phenyl groups. Both of these phenomena function to lower the dissociation energy of bridged carboxylates thereby increasing the surface reactivity. Additionally, the ligands were found to direct different growth rates in thermolysis reactions using the clusters as single source precursors by hindering the rate of surface addition to extend the nucleation period. Taking advantage of the surface rigidity imparted by meta-substituents in lower temperature thermolysis reactions allowed for the isolation and characterization of InP-419, an intermediate in the dissolution of $\text{In}_{37}\text{P}_{20}$. We conclude that this species is borne of indium carboxylate loss and shows structural similarities to a computationally predicted InP cluster.¹¹ The mapping of relationships between these reactions is summarized in **Figure 8**.

Finally, we have leveraged the diffusion control and stability of the 4-*tert*-butylphenylacetate ligand to kinetically trap an intermediate InP cluster fragment. Complete structural characterization was carried out by SCXRD confirming the identity of the fragment to be $\text{In}_{26}\text{P}_{13}(\text{O}_2\text{CR})_{39}$ and allowed for the observation that the core of this cluster fragment is homologous to the $\text{Cd}_{14}\text{Se}_{13}$ cluster ligated with TMEDA and chloride.

These observations have powerful implications for control over cluster-based nanocrystal systems and act as the first definitive evidence for the structural similarities between III-V and II-VI clusters.

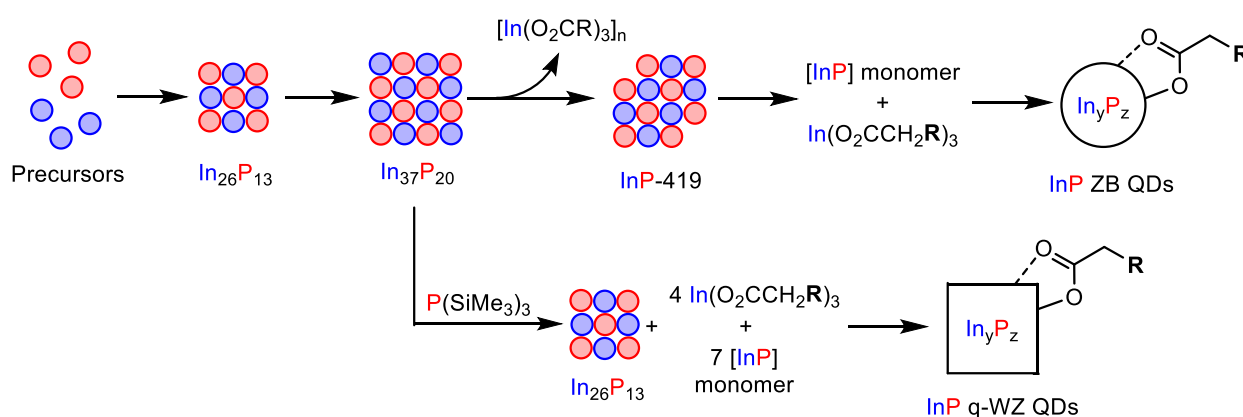


Figure 8. Summary of investigated reaction pathways of InP magic-sized clusters. The $\text{In}_{26}\text{P}_{13}$ cluster precedes formation of $\text{In}_{37}\text{P}_{20}$ which then undergoes dissolution through InP-419 to generate monomers to renucleate zinc-blende QDs. The addition of $\text{P}(\text{SiMe}_3)_3$ to $\text{In}_{37}\text{P}_{20}$ induces fragmentation to form $\text{In}_{26}\text{P}_{13}$ which is the nucleus from which quasi-wurtzite QDs are grown.

Acknowledgments

This work was supported by the National Science Foundation under grant CHE-2107237. PDF characterization was completed in collaboration with support from the National Science Foundation under Grant No. DMR-2019444. Part of this work was conducted at the Washington Nanofabrication Facility / Molecular Analysis Facility, a National Nanotechnology Coordinated Infrastructure (NNCI) site at the University of Washington with partial support from the National Science Foundation *via* awards NNCI-1542101 and NNCI-2025489. X-ray total scattering experiments were completed at Beamline 28-ID-1 (PDF) of the National Synchrotron Light Source II, a U.S. Department of Energy (DOE) Office of Science User Facility operated for the DOE Office of Science by Brookhaven National Laboratory under Contract No. DE-SC0012704. We gratefully acknowledge PhD student Hao Nguyen for design of the TOC graphic.

Supporting Information

Complete experimental methods and supplementary data (NMR, PDF, Raman, FTIR, UV-Vis, kinetics, global fits, pXRD, TEM, crystallographic tables, and DFT calculations).

References

- (1) Kim, Y.; Ham, S.; Jang, H.; Min, J. H.; Chung, H.; Lee, J.; Kim, D.; Jang, E. Bright and Uniform Green Light Emitting InP/ZnSe/ZnS Quantum Dots for Wide Color Gamut Displays. *ACS Appl. Nano Mater.* **2019**, *2* (3), 1496–1504. <https://doi.org/10.1021/acsnm.8b02063>.
- (2) Won, Y.-H.; Cho, O.; Kim, T.; Chung, D.-Y.; Kim, T.; Chung, H.; Jang, H.; Lee, J.; Kim, D.; Jang, E. Highly Efficient and Stable InP/ZnSe/ZnS Quantum Dot Light-Emitting Diodes. *Nature* **2019**, *575* (7784), 634–638. <https://doi.org/10.1038/s41586-019-1771-5>.
- (3) Gary, D. C.; Terban, M. W.; Billinge, S. J. L.; Cossairt, B. M. Two-Step Nucleation and Growth of InP Quantum Dots via Magic-Sized Cluster Intermediates. *Chem. Mater.* **2015**, *27* (4), 1432–1441. <https://doi.org/10.1021/acs.chemmater.5b00286>.
- (4) Friedfeld, M. R.; Johnson, D. A.; Cossairt, B. M. Conversion of InP Clusters to Quantum Dots. *Inorg. Chem.* **2019**, *58* (1), 803–810. <https://doi.org/10.1021/acs.inorgchem.8b02945>.
- (5) Xie, L.; Shen, Y.; Franke, D.; Sebastián, V.; Bawendi, M. G.; Jensen, K. F. Characterization of Indium Phosphide Quantum Dot Growth Intermediates Using MALDI-TOF Mass

- Spectrometry. *J. Am. Chem. Soc.* **2016**, *138* (41), 13469–13472.
<https://doi.org/10.1021/jacs.6b06468>.
- (6) McMurtry, B. M.; Qian, K.; Teglassi, J. K.; Swarnakar, A. K.; De Roo, J.; Owen, J. S. Continuous Nucleation and Size Dependent Growth Kinetics of Indium Phosphide Nanocrystals. *Chem. Mater.* **2020**, *32* (10), 4358–4368.
<https://doi.org/10.1021/acs.chemmater.0c01561>.
 - (7) Gary, D. C.; Flowers, S. E.; Kaminsky, W.; Petrone, A.; Li, X.; Cossairt, B. M. Single-Crystal and Electronic Structure of a 1.3 Nm Indium Phosphide Nanocluster. *J. Am. Chem. Soc.* **2016**, *138* (5), 1510–1513. <https://doi.org/10.1021/jacs.5b13214>.
 - (8) Friedfeld, M. R.; Stein, J. L.; Johnson, D. A.; Park, N.; Henry, N. A.; Enright, M. J.; Mocatta, D.; Cossairt, B. M. Effects of Zn²⁺ and Ga³⁺ Doping on the Quantum Yield of Cluster-Derived InP Quantum Dots. *J. Chem. Phys.* **2019**, *151* (19), 194702.
<https://doi.org/10.1063/1.5126971>.
 - (9) Ritchhart, A.; Cossairt, B. M. Templated Growth of InP Nanocrystals with a Polytwistane Structure. *Angewandte Chemie International Edition* **2018**, *57* (7), 1908–1912.
<https://doi.org/10.1002/anie.201711539>.
 - (10) Zhao, Q.; Kulik, H. J. Electronic Structure Origins of Surface-Dependent Growth in III–V Quantum Dots. *Chem. Mater.* **2018**, *30* (20), 7154–7165.
<https://doi.org/10.1021/acs.chemmater.8b03125>.
 - (11) Shim, D.; Kang, J. Enhanced Reactivity of Magic-Sized Inorganic Clusters by Engineering the Surface Ligand Networks. *Chem. Mater.* **2023**, *35* (2), 700–708.
<https://doi.org/10.1021/acs.chemmater.2c03394>.
 - (12) Williamson, C. B.; Nevers, D. R.; Nelson, A.; Hadar, I.; Banin, U.; Hanrath, T.; Robinson, R. D. Chemically Reversible Isomerization of Inorganic Clusters. *Science* **2019**, *363* (6428), 731–735. <https://doi.org/10.1126/science.aau9464>.
 - (13) Shim, D.; Lee, J.; Kang, J. Multiscale Isomerization of Magic-Sized Inorganic Clusters Chemically Driven by Atomic-Bond Exchanges. *Chem. Mater.* **2022**, *34* (21), 9527–9535.
<https://doi.org/10.1021/acs.chemmater.2c02018>.
 - (14) Bootharaju, M. S.; Baek, W.; Deng, G.; Singh, K.; Voznyy, O.; Zheng, N.; Hyeon, T. Structure of a Subnanometer-Sized Semiconductor Cd₁₄Se₁₃ Cluster. *Chem* **2022**, *8* (11), 2978–2989. <https://doi.org/10.1016/j.chempr.2022.06.025>.
 - (15) Köhl, O. The Range of Chemical Shifts, Coupling Constants, and What Influences Each. In *Phosphorus-31 NMR Spectroscopy: A Concise Introduction for the Synthetic Organic and Organometallic Chemist*; Köhl, O., Ed.; Springer Berlin Heidelberg: Berlin, Heidelberg, 2008; pp 7–23. https://doi.org/10.1007/978-3-540-79118-8_2.
 - (16) Tolman, C. A. Steric Effects of Phosphorus Ligands in Organometallic Chemistry and Homogeneous Catalysis. *Chem. Rev.* **1977**, *77* (3), 313–348.
<https://doi.org/10.1021/cr60307a002>.
 - (17) Marion, D. An Introduction to Biological NMR Spectroscopy. *Mol Cell Proteomics* **2013**, *12* (11), 3006–3025. <https://doi.org/10.1074/mcp.O113.030239>.
 - (18) Juhás, P.; Davis, T.; Farrow, C. L.; Billinge, S. J. L. PDFgetX3: A Rapid and Highly Automatable Program for Processing Powder Diffraction Data into Total Scattering Pair Distribution Functions. *J Appl Cryst* **2013**, *46* (2), 560–566.
<https://doi.org/10.1107/S0021889813005190>.

- (19) Bedel, E.; Landa, G.; Carles, R.; Redoules, J. P.; Renucci, J. B. Raman Investigation of the InP Lattice Dynamics. *J. Phys. C: Solid State Phys.* **1986**, *19* (10), 1471–1479. <https://doi.org/10.1088/0022-3719/19/10/004>.
- (20) Vasilevsky, M. I.; Rolo, A. G.; Gomes, M. J. M.; Gaponik, N. P.; Talapin, D. V.; Rogach, A. L. Raman and FIR Studies of Optical Phonons Confined in InP Quantum Dots. In *Conference Proceedings. 14th Indium Phosphide and Related Materials Conference (Cat. No.02CH37307)*; 2002; pp 67–70. <https://doi.org/10.1109/ICIPRM.2002.1014108>.
- (21) Seong, M. J.; Mičić, O. I.; Nozik, A. J.; Mascarenhas, A.; Cheong, H. M. Size-Dependent Raman Study of InP Quantum Dots. *Applied Physics Letters* **2003**, *82* (2), 185–187. <https://doi.org/10.1063/1.1535272>.
- (22) Beecher, A. N.; Dziatko, R. A.; Steigerwald, M. L.; Owen, J. S.; Crowther, A. C. Transition from Molecular Vibrations to Phonons in Atomically Precise Cadmium Selenide Quantum Dots. *J. Am. Chem. Soc.* **2016**, *138* (51), 16754–16763. <https://doi.org/10.1021/jacs.6b10705>.
- (23) Huang, M.; Yan, H.; Heinz, T. F.; Hone, J. Probing Strain-Induced Electronic Structure Change in Graphene by Raman Spectroscopy. *Nano Lett.* **2010**, *10* (10), 4074–4079. <https://doi.org/10.1021/nl102123c>.
- (24) Neumann, C.; Reichardt, S.; Venezuela, P.; Drögeler, M.; Banszerus, L.; Schmitz, M.; Watanabe, K.; Taniguchi, T.; Mauri, F.; Beschoten, B.; Rotkin, S. V.; Stampfer, C. Raman Spectroscopy as Probe of Nanometre-Scale Strain Variations in Graphene. *Nat Commun* **2015**, *6* (1), 8429. <https://doi.org/10.1038/ncomms9429>.
- (25) Huang, M.; Yan, H.; Chen, C.; Song, D.; Heinz, T. F.; Hone, J. Phonon Softening and Crystallographic Orientation of Strained Graphene Studied by Raman Spectroscopy. *Proceedings of the National Academy of Sciences* **2009**, *106* (18), 7304–7308. <https://doi.org/10.1073/pnas.0811754106>.
- (26) Leger, J. D.; Friedfeld, M. R.; Beck, R. A.; Gaynor, J. D.; Petrone, A.; Li, X.; Cossairt, B. M.; Khalil, M. Carboxylate Anchors Act as Exciton Reporters in 1.3 Nm Indium Phosphide Nanoclusters. *J. Phys. Chem. Lett.* **2019**, *10* (8), 1833–1839. <https://doi.org/10.1021/acs.jpcclett.9b00602>.
- (27) Klein, M. D.; Bisted, C. H.; Dou, F. Y.; Sandwisch, J. W.; Cossairt, B. M.; Khalil, M. Measuring Relative Energies of Ligand Binding Conformations on Nanocluster Surfaces with Temperature-Dependent FTIR Spectroscopy. *J. Phys. Chem. C* **2023**. <https://doi.org/10.1021/acs.jpcc.3c03951>.
- (28) Zelenák, V.; Vargová, Z.; Györyová, K. Correlation of Infrared Spectra of Zinc(II) Carboxylates with Their Structures. *Spectrochimica Acta Part A: Molecular and Biomolecular Spectroscopy* **2007**, *66* (2), 262–272. <https://doi.org/10.1016/j.saa.2006.02.050>.
- (29) Chakravarty, C.; Debenedetti, P. G.; Stillinger, F. H. Lindemann Measures for the Solid-Liquid Phase Transition. *The Journal of Chemical Physics* **2007**, *126* (20), 204508. <https://doi.org/10.1063/1.2737054>.
- (30) Battaglia, D.; Peng, X. Formation of High Quality InP and InAs Nanocrystals in a Noncoordinating Solvent. *Nano Lett.* **2002**, *2* (9), 1027–1030. <https://doi.org/10.1021/nl025687v>.
- (31) Lucey, D. W.; MacRae, D. J.; Furis, M.; Sahoo, Y.; Cartwright, A. N.; Prasad, P. N. Monodispersed InP Quantum Dots Prepared by Colloidal Chemistry in a Noncoordinating Solvent. *Chem. Mater.* **2005**, *17* (14), 3754–3762. <https://doi.org/10.1021/cm050110a>.

- (32) Ouyang, J.; Kuijper, J.; Brot, S.; Kingston, D.; Wu, X.; Leek, D. M.; Hu, M. Z.; Ripmeester, J. A.; Yu, K. Photoluminescent Colloidal CdS Nanocrystals with High Quality via Noninjection One-Pot Synthesis in 1-Octadecene. *J. Phys. Chem. C* **2009**, *113* (18), 7579–7593. <https://doi.org/10.1021/jp900252e>.
- (33) *Controlling the Size of Hot Injection Made Nanocrystals by Manipulating the Diffusion Coefficient of the Solute*. <https://doi.org/10.1021/ja509941g>.
- (34) Dümbgen, K. C.; Zito, J.; Infante, I.; Hens, Z. Shape, Electronic Structure, and Trap States in Indium Phosphide Quantum Dots. *Chem. Mater.* **2021**, *33* (17), 6885–6896. <https://doi.org/10.1021/acs.chemmater.1c01795>.
- (35) Ripberger, H.; Schnitzenbaumer, K.; Nguyen, L.; Ladd, D.; Levine, K.; Dayton, D.; Toney, M.; Cossairt, B. Navigating the Potential Energy Surface of CdSe Magic-Sized Clusters: Synthesis and Interconversion of Atomically Precise Nanocrystal Polymorphs. ChemRxiv August 16, 2023. <https://doi.org/10.26434/chemrxiv-2023-jzwm3>.
- (36) Ma, F.; Abboud, K. A.; Zeng, C. Precision Synthesis of a CdSe Semiconductor Nanocluster via Cation Exchange. *Nat. Synth* **2023**, 1–11. <https://doi.org/10.1038/s44160-023-00330-6>.
- (37) Deveson, A.; Dehnen, S.; Fenske, D. Syntheses and Structures of Four New Copper(I)–Selenium Clusters: Size Dependence of the Cluster on the Reaction Conditions. *J. Chem. Soc., Dalton Trans.* **1997**, No. 23, 4491–4498. <https://doi.org/10.1039/A705750D>.